

Ground-State Phase Diagram of an Anisotropic $S=1/2$ Ladder with Different Leg Interactions

Takashi Tonegawa^{1,2*}, Toshiya Hikihara³, Kiyomi Okamoto⁴, Shunsuke C. Furuya⁵, and Tôru Sakai^{6,7}

¹*Professor Emeritus, Kobe University, Kobe 657-8501, Japan*

²*Department of Physical Science, Osaka Prefecture University, Sakai 599-8531, Japan*

³*Faculty of Science and Technology, Gunma University, Kiryu 376-8515, Japan*

⁴*College of Engineering, Shibaura Institute of Technology, Saitama 337-8570, Japan*

⁵*Condensed Matter Theory Laboratory, RIKEN, Wako 351-0198, Japan*

⁶*Graduate School of Material Science, University of Hyogo, Hyogo 678-1297, Japan*

⁷*National Institutes for Quantum and Radiological Science and Technology (QST), SPring-8, Hyogo 679-5148, Japan*

We explore the ground-state phase diagram of the $S=1/2$ two-leg ladder with different leg interactions. The xy - and z -components of the leg interactions between nearest-neighbor spins in the a (b) leg are respectively denoted by $J_{1,a}$ and $\Delta_1 J_{1,a}$ ($J_{1,b}$ and $\Delta_1 J_{1,b}$). On the other hand, the xy - and z -components of the uniform rung interactions are respectively denoted by $\Gamma_r J_r$ and J_r . In the above, Δ_1 and Γ_r are the XXZ -type anisotropy parameters for the leg and rung interactions, respectively. This system has frustration when $J_{1,a} J_{1,b} < 0$ irrespective of the sign of J_r . The phase diagram on the Δ_1 ($|\Delta_1| \leq 1.0$) versus $J_{1,b}$ ($-2.0 \leq J_{1,b} \leq 3.0$) plane in the case where $J_{1,a} = 0.2$, $J_r = -1.0$, and $\Gamma_r = 0.5$ is determined numerically. We employ physical considerations and perform level spectroscopy and phenomenological renormalization-group analyses of the numerical data obtained by the exact diagonalization method. The resultant phase diagram contains the ferromagnetic, Haldane, Néel, nematic Tomonaga-Luttinger liquid (TLL), partial ferrimagnetic, and $XY1$ phases. Interestingly enough, the nematic TLL phase appears in the strong-rung unfrustrated region as well as in the strong-rung frustrated region. We perform first-order perturbational calculations from the strong-rung coupling limit to elucidate the characteristic features of the phase diagram. Furthermore, we carry out density-matrix renormalization-group calculations for some physical quantities such as the energy gaps, the local magnetization, and the spin correlation functions to supplement the reliability of the phase diagram. The phase diagram on the Γ_r ($0.0 \leq \Gamma_r \leq 1.0$) versus $J_{1,b}$ ($-1.0 \leq J_{1,b} \leq 2.0$) plane in the case where $J_{1,a} = 0.2$, $J_r = -1.0$, and $\Delta_1 = 1.0$ is also discussed briefly.

KEYWORDS: ground-state phase diagram, anisotropic $S=1/2$ ladder, different leg interactions, nematic Tomonaga-Luttinger liquid phase, exact diagonalization calculation, perturbational calculation, density-matrix renormalization-group calculation

1. Introduction

Over the past several decades, a great deal of effort has been devoted to clarifying the frustration effect on the ground-state properties of low-dimensional quantum spin systems with competing interactions. It is now well known experimentally as well as theoretically and numerically that a reciprocal influence between the strong quantum fluctuation and the geometrical frustration in these systems induces various exotic quantum ground states such as the dimer state accompanying spontaneous translational symmetry breaking, the spin-nematic Tomonaga-Luttinger liquid (TLL) state, and so on. The former state is realized in an $S=1/2$ zigzag chain with antiferromagnetic nearest-neighbor (nn) and next-nearest-neighbor (nnn) interactions.¹⁻⁶ On the other hand, the latter state is realized in an anisotropic $S=1$ chain,⁷⁻⁹ in an $S=1$ chain with bilinear and biquadratic interactions,¹⁰ and in an $S=1/2$ zigzag chain with ferromagnetic nn and antiferromagnetic nnn interactions under an external magnetic field.¹¹⁻¹³

In the case of an $S=1/2$ two-leg ladder system,

the frustration is usually introduced by adding nnn leg and/or diagonal interactions to an original system with nn leg and rung interactions, as has been extensively investigated.¹⁴⁻¹⁶ As another example, an $S=1/2$ ladder with uniform nn leg and alternating rung interactions has also been studied by several authors.¹⁷⁻¹⁹ We¹⁹ have discussed the ground-state phase diagram in the frustrated case where rung interactions are ferromagnetically-antiferromagnetically alternating and have a common Ising-type anisotropy, while leg interactions are antiferromagnetically uniform and isotropic. Our results show that, when the leg interactions are relatively weak compared with the rung interactions, the incommensurate Haldane state as well as the commensurate one appears as the ground state in the whole range of the Ising-type anisotropy parameter. This appearance of the Haldane state in the case where the Ising character of rung interactions is strong is contrary to the ordinary situation, and is called the inversion phenomenon concerning the interaction anisotropy.²⁰⁻²³

In the present paper, we explore the ground-state phase diagram of an anisotropic $S=1/2$ ladder with different leg interactions, which is schematically sketched in

*E-mail address: tone0115@vivid.ocn.ne.jp

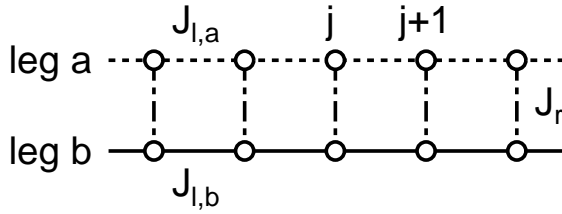


Fig. 1. Schematic sketch of the $S=1/2$ ladder with different leg interactions. Open circles denote $S=1/2$ spins, while solid, dotted and dot-dashed lines denote, respectively, the interaction constants, $J_{1,a}$, $J_{1,b}$, and J_r .

Fig. 1 and described by the Hamiltonian

$$\begin{aligned} \mathcal{H} = & J_{1,a} \sum_{j=1}^L \{ S_{j,a}^x S_{j+1,a}^x + S_{j,a}^y S_{j+1,a}^y + \Delta_1 S_{j,a}^z S_{j+1,a}^z \} \\ & + J_{1,b} \sum_{j=1}^L \{ S_{j,b}^x S_{j+1,b}^x + S_{j,b}^y S_{j+1,b}^y + \Delta_1 S_{j,b}^z S_{j+1,b}^z \} \\ & + J_r \sum_{j=1}^L \{ \Gamma_r (S_{j,a}^x S_{j,b}^x + S_{j,a}^y S_{j,b}^y) + S_{j,a}^z S_{j,b}^z \}. \quad (1) \end{aligned}$$

Here, $S_{j,\ell}^x$, $S_{j,\ell}^y$, and $S_{j,\ell}^z$ are, respectively, the x -, y -, and z -components of the $S=1/2$ operator $\vec{S}_{j,\ell}$ at the (j, ℓ) site assigned by the j th rung and the $\ell (= a \text{ or } b)$ leg; $J_{1,a}$ and $J_{1,b}$ denote, respectively, the magnitudes of the a leg and b leg interactions, while J_r denotes that of the rung interaction; Δ_1 and Γ_r are, respectively, the parameters representing the XXZ -type anisotropies of the former and latter interactions; L is the total number of rungs, which is assumed to be even. It is emphasized that this system has frustration when $J_{1,a}J_{1,b} < 0$ irrespective of the sign of J_r .

It is unfortunate that real materials for which the above \mathcal{H} is a good model Hamiltonian have been neither synthesized nor found so far. We do not think, however, that it is physically unrealistic. Actually, Yamaguchi *et al.*^{24, 25)} have recently demonstrated the modulation of magnetic interactions in spin ladder systems by using verdazyl-radical crystals. The flexibility of molecular arrangements in such organic-radical materials is expected to realize $S=1/2$ ladder systems with different leg interactions.

Our Hamiltonian \mathcal{H} contains five interaction parameters. Throughout the following discussions, we focus our attention upon the case where $J_{1,a}=0.2$, $-2.0 \leq J_{1,b} \leq 3.0$, $J_r = -1.0$, $|\Delta_1| \leq 1.0$, and $\Gamma_r = 0.5$, unless otherwise stated. Here, we choose $|J_r|$ as the unit of energy. It is noted that the anisotropies of the leg and rung interactions are, respectively, of the XY and Ising types. The motivation for treating this case is as follows. When the ferromagnetic rung interactions with Ising-type anisotropy are much stronger than both kinds of leg interactions ($|J_{1,b}| \ll 1.0$), a pair of $S=1/2$ spins at each rung forms a bound state of two magnons with $S_{j,a}^z + S_{j,b}^z = \pm 1$. This may lead to the nematic TLL state, which accompanies two-magnon bound states, as the

ground state at least in the frustrated region. Furthermore, the XY -type anisotropy of the leg interactions is expected to stabilize the nematic TLL state.

In this paper, we use the term ‘‘nematic TLL’’ for the TLL characterized not only by the formation of two-magnon bound pairs but also by the dominant nematic four-spin correlation function. In the nematic TLL state composed of the bosons of two-magnon bound pairs,^{7, 12)} the nematic four-spin and longitudinal two-spin correlations are dual to each other, and the decay exponent of the former, η^{++--} , and that of the latter, η_ℓ^{zz} , obey the relation $\eta^{++--}\eta_\ell^{zz} = 1$. [See Eqs. (38) and (37) for the definitions of η^{++--} and η_ℓ^{zz} , respectively.] If $\eta^{++--} < 1$, the nematic correlation is dominant, leading to the nematic TLL state defined above. On the other hand, the TLL state with the dominant longitudinal two-spin correlation is not allowed in the present system, since, if $\eta_\ell^{zz} < 1$, the Umklapp scattering becomes relevant and the TLL state turns into the Néel state. The situation is distinct from that of zigzag chains under a magnetic field, in which the TLL state accompanied with two-magnon bound pairs and dominant incommensurate spin-density-wave correlation appears in wide regions of the magnetic phase diagrams.^{12, 13, 26, 27)}

We note, at this junction, that ground states of the ladder system governed by the Hamiltonian \mathcal{H} have already been discussed in a few other cases.^{28–30)} We²⁹⁾ have determined the ground-state phase diagram on the $1/\Gamma_r$ ($\Gamma_r \geq 1.0$) versus $J_{1,b}$ plane in the case where $J_{1,a} = \pm 0.2$, $J_r \Gamma_r = -1.0$, and $\Delta_1 = 1.0$. The obtained phase diagrams consist of the $XY1$ phase, the triplet-dimer phase, the partial ferrimagnetic phase (which is called the non-collinear ferrimagnetic phase in the paper), and the Haldane phase. Interestingly, the direct-product triplet-dimer state becomes to be the exact ground state^{28, 31)} when $J_{1,b} = -J_{1,a}$ and $\Gamma_r \gtrsim 1.2$. On the other hand, extending Tsukano and Takahashi’s work,²⁸⁾ Sekiguchi and Hida³⁰⁾ have shown, in the case where $J_{1,a}J_{1,b} < 0$ and $\Delta_1 = \Gamma_r = 1.0$, that the partial ferrimagnetic state, which is a spontaneously magnetized TLL state with incommensurate magnetic correlation, appears as the ground state over a wide parameter range.

The remainder of this paper is organized as follows. In Sect. 2, with the help of physical considerations we numerically determine, by using the exact diagonalization (ED) method, the ground-state phase diagram on the Δ_1 versus $J_{1,b}$ plane in the case where $J_{1,a} = 0.2$, $J_r = -1.0$, and $\Gamma_r = 0.5$. In Sect. 3, we show that the distinguishing features of the obtained phase diagram are well explained by performing perturbational calculations. In Sect. 4, in order to supplement the reliability of the phase diagram, we carry out density-matrix renormalization-group (DMRG) calculations^{32, 33)} for some physical quantities such as the energy gaps, the local magnetization, and the spin correlation functions. The final section (Sect. 5) contains concluding remarks. In Appendix, the ground-state phase diagram on the Γ_r versus $J_{1,b}$ plane in the case where $J_{1,a} = 0.2$, $J_r = -1.0$, and $\Delta_1 = 1.0$ is briefly discussed.

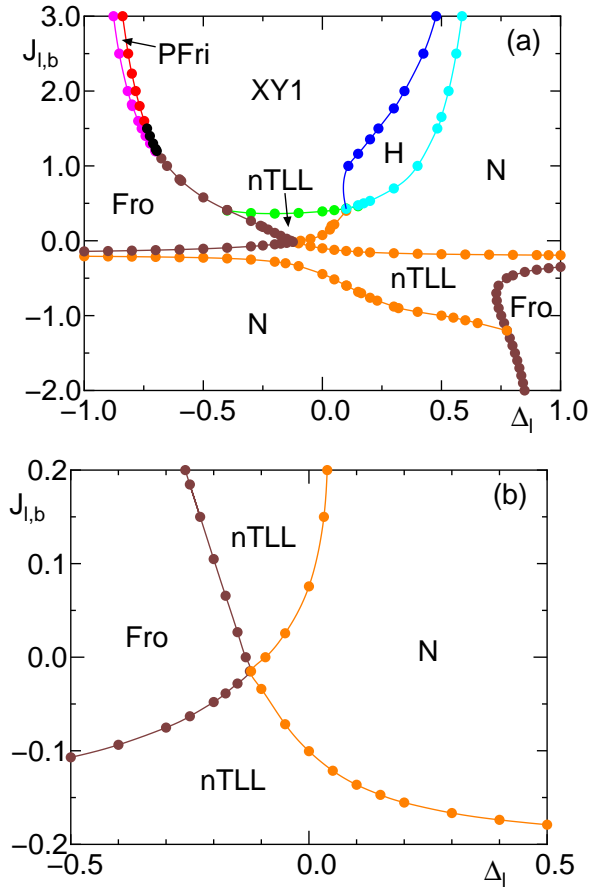


Fig. 2. (Color online) Ground-state phase diagram on the Δ_1 versus $J_{1,b}$ plane in the case where $J_{1,a}=0.2$, $J_r=-1.0$, and $\Gamma_r=0.5$, obtained in the present work. In (a) the whole view is shown, while in (b) an enlarged view around the origin is given. The regions designated by Fro, PFri, XY1, H, N, and nTLL are those of the ferromagnetic, partial ferrimagnetic, XY1, Haldane, Néel, and nematic TLL phases, respectively.

2. Numerical Determination of the Ground-State Phase Diagram

In this section we present the result for the ground-state phase diagram on the Δ_1 versus $J_{1,b}$ plane in the case where $J_{1,a}=0.2$, $J_r=-1.0$, and $\Gamma_r=0.5$, which has been determined by using a variety of numerical methods based on the ED calculation. First of all, we show the obtained phase diagram in Fig. 2. This phase diagram consists of six kinds of phases; these are the ferromagnetic, partial ferrimagnetic, XY1, Haldane, Néel, and nematic TLL phases. It is noted that the nematic TLL phase appears as the ground state in the strong-rung frustrated region ($-1.0 \lesssim J_{1,b} < 0.0$), as is expected, and survives even in the strong-rung unfrustrated region ($0.0 \leq J_{1,b} \lesssim 0.4$).

Before explaining how to numerically determine the phase boundary lines, we introduce some related physical quantities. We denote, respectively, by $E_0^P(L, M)$ and $E_1^P(L, M)$, the lowest- and second-lowest-energy eigenvalues of the Hamiltonian \mathcal{H} under the periodic boundary condition (PBC), $\vec{S}_{L+1,\ell} = \vec{S}_{1,\ell}$, within the subspace characterized by L and the total magnetization

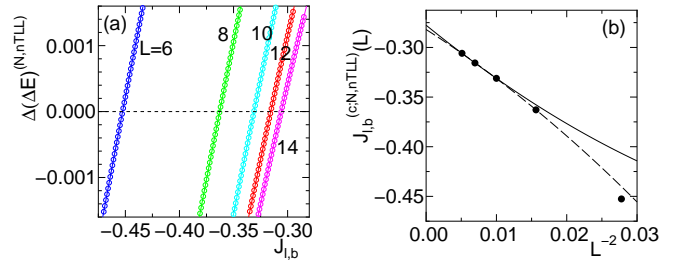


Fig. 3. (Color online) (a) Plot of $\Delta(\Delta E)^{(N,nTLL)}[\equiv \Delta E_1^P(L, 0) - \frac{1}{2}\Delta E_0^P(L, 2)]$ versus $J_{1,b}$ for $\Delta_1 = -0.2$ and for $L=6$ (blue), $L=8$ (green), $L=10$ (cyan), $L=12$ (red), and $L=14$ (magenta). The finite-size critical value $J_{1,b}^{(c;N,nTLL)}(L)$ for each L is the value of $J_{1,b}$ at which $\Delta(\Delta E)^{(N,nTLL)} = 0$ is satisfied. (b) Plot of $J_{1,b}^{(c;N,nTLL)}(L)$ versus L^{-2} for $\Delta_1 = -0.2$. The solid and dashed lines represent, respectively, the least-squares fittings where the data from $L=10$ to $L=14$ and the data from $L=8$ to $L=14$ are used. These extrapolations give the result $J_{1,b}^{(c;N,nTLL)} = -0.280 \pm 0.002$ at the $L \rightarrow \infty$ limit, where the numerical error is estimated from the difference between the above two extrapolated results.

$M \equiv \sum_{j=1}^L (S_{j,a}^z + S_{j,b}^z)$. Here, M is a good quantum number with the eigenvalues of $M = 0, \pm 1, \dots, \pm L$. Furthermore, the quantity $E_0^T(L, M)$ is the lowest-energy eigenvalue of \mathcal{H} under the twisted boundary condition (TBC), $S_{L+1,\ell}^x = -S_{1,\ell}^x$, $S_{L+1,\ell}^y = -S_{1,\ell}^y$, and $S_{L+1,\ell}^z = S_{1,\ell}^z$, within the subspace determined by L and M . Then, we define several energy differences as follows:

$$\Delta E_0^P(L, M) = E_0^P(L, M) - E_0^P(L, 0), \quad (2)$$

$$\Delta E_1^P(L, 0) = E_1^P(L, 0) - E_0^P(L, 0), \quad (3)$$

$$\Delta E_0^T(L, 0) = E_0^T(L, 0) - E_0^P(L, 0). \quad (4)$$

It is noted that the values of the ground-state magnetization $M_g(L)$ are $M_g(L) = L$, $0 < M_g(L) < L$, and $M_g(L) = 0$ in the ferromagnetic, partial ferrimagnetic, and remaining four phases, respectively.

Let us first discuss the phase boundary lines between the Néel and nematic TLL phases, which are depicted by the brown lines in Fig. 2. It should be emphasized that the nematic TLL state is the TLL state which accompanies two-magnon bound states and is equivalent to the XY2 state, originally proposed by Schulz.⁷⁾ The corresponding phase transition is of the Berezinskii-Kosterlitz-Thouless (BKT) type^{34,35)} accompanying the spontaneous translational-symmetry breaking (STSB), and therefore, as is well known, the phase boundary line can be accurately estimated by the level spectroscopy (LS) method developed by Okamoto and Nomura.^{3,5,6)} In this method, the difficulty coming from the logarithmic-correction problem associated with the BKT transition is removed. According to this method, the critical value $J_{1,b}^{(c;N,nTLL)}$ of $J_{1,b}$ for a given value of Δ_1 can be evaluated as follows. We numerically solve the equation

$$\Delta E_1^P(L, 0) = \frac{1}{2} \Delta E_0^P(L, 2), \quad (5)$$

to compute the finite-size critical value $J_{1,b}^{(c;N,nTLL)}(L)$ for

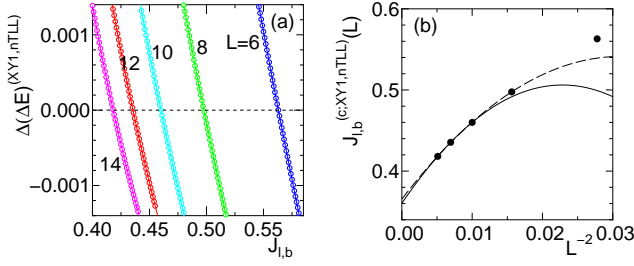


Fig. 4. (Color online) (a) Plot of $\Delta(\Delta E)^{(XY1,nTLL)}[\equiv \Delta E_0^P(L, 1) - \frac{1}{2}\Delta E_0^P(L, 2)]$ versus $J_{1,b}$ for $\Delta_1 = -0.2$. The correspondence of the color of each line to the value of each L is the same as that in Fig. 3(a). (b) Plot of $J_{1,b}^{(c;XY1,nTLL)}(L)$ versus L^{-2} for $\Delta_1 = -0.2$. The meanings of the solid and dashed lines are the same as those in Fig. 3(b). The extrapolated value to $L \rightarrow \infty$ is given by $J_{1,b}^{(c;XY1,nTLL)} = 0.363 \pm 0.003$.

various values of L . Then, we extrapolate these finite-size results to the thermodynamic ($L \rightarrow \infty$) limit. Practically, we have carried out the ED calculation to compute $J_{1,b}^{(c;N,nTLL)}(L)$ for finite- L systems with $L=6, 8, \dots, 14$ rungs. Performing the $L \rightarrow \infty$ extrapolation of $J_{1,b}^{(c;N,nTLL)}(L)$'s, we have fitted them to quadratic functions of L^{-2} by using the least-squares method. An example of the results is $J_{1,b}^{(c;N,nTLL)} = -0.280 \pm 0.002$ for $\Delta_1 = -0.2$. These procedures for the evaluation of $J_{1,b}^{(c;N,nTLL)}$ are illustrated in Fig. 3. The phase boundary lines are drawn by plotting $J_{1,b}^{(c;N,nTLL)}$'s as functions of Δ_1 .

In the following discussion in this section, we mainly describe how to compute the finite-size critical values only, since the evaluation of the critical value at the thermodynamic limit has been done in the same way.

Secondly (see the green line in Fig. 2), we discuss the phase boundary line between the XY1 and nematic TLL phases. The nematic TLL state accompanies two-magnon bound states, as mentioned above, while the XY1 state does not. These lead to the following fact. In the ground-state magnetization curve for a given finite-size system under an external magnetic field \vec{H} applied along the z -axis, the magnetization increases stepwisely with increasing $|\vec{H}|$; the first step occurs from the $M_g(L)=0$ state to the $M_g(L)=2$ state in the nematic TLL phase, while it occurs from the $M_g(L)=0$ state to the $M_g(L)=1$ state in the XY1 phase. From these arguments, it is easy to see that the finite-size critical value $J_{1,b}^{(c;XY1,nTLL)}(L)$ of $J_{1,b}$, for a given value of Δ_1 , for the phase transition between the XY1 and nematic TLL phases is calculated by solving

$$\Delta E_0^P(L, 1) = \frac{1}{2} \Delta E_0^P(L, 2) \quad (6)$$

numerically. Figure 4 shows the determination of the critical value $J_{1,b}^{(c;XY1,nTLL)}$ at the thermodynamic limit for $\Delta_1 = -0.2$.

Thirdly (the blue line in Fig. 2), the phase transition between the XY1 and Haldane phases is the BKT transition without the STSB. It is also well known that, in this

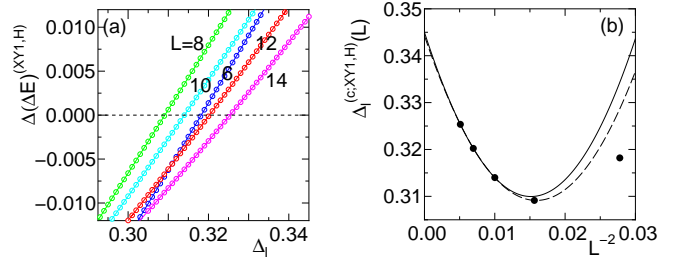


Fig. 5. (Color online) (a) Plot of $\Delta(\Delta E)^{(XY1,H)}[\equiv \Delta E_0^P(L, 2) - \Delta E_0^T(L, 0)]$ versus Δ_1 for $J_{1,b} = 2.0$. The correspondence of the color of each line to the value of each L is the same as that in Fig. 3(a). (b) Plot of $\Delta_1^{(c;XY1,H)}(L)$ versus L^{-2} for $J_{1,b} = 2.0$. The meanings of the solid and dashed lines are the same as those in Fig. 3(b). The extrapolated value to $L \rightarrow \infty$ is given by $\Delta_1^{(c;XY1,H)} = 0.345 \pm 0.001$.

case, Nomura and Kitazawa's LS method,³⁶⁾ in which the difficulty coming from the logarithmic-correction problem is also removed, is very powerful for determining the phase boundary line. The finite-size critical value $\Delta_1^{(c;XY1,H)}(L)$ of Δ_1 for a given value of $J_{1,b}$ is calculated by using the equation

$$\Delta E_0^P(L, 2) = \Delta E_0^T(L, 0). \quad (7)$$

In Fig. 5 we show the determination of the critical value $\Delta_1^{(c;XY1,H)}$ at the thermodynamic limit for $J_{1,b} = 2.0$.

Fourthly (the umber lines in Fig. 2), the phase transitions between the ferromagnetic phase and one of the XY1, Néel, and nematic TLL phases are of the first-order, because these transitions are between the $M_g(L) = L$ and $M_g(L) = 0$ states at the $L \rightarrow \infty$ limit. Thus, it is apparent that the phase boundary lines are obtained from the equation

$$\Delta E_0^P(L, L) = 0. \quad (8)$$

As an example, we discuss here the phase transition between the ferromagnetic and nematic TLL phases in the case of $J_{1,b} = -0.7$, denoting the finite-size critical value by $\Delta_1^{(c;Fro,nTLL)}(L)$. In Fig. 6 the determination of the critical value $\Delta_1^{(c;Fro,nTLL)}$ at the thermodynamic limit in this case is illustrated.

Fifthly (the magenta, red, and black lines in Fig. 2), according to the result of our calculations, the partial ferrimagnetic phase appears in a rather narrow region of Δ_1 , which lies between the ferromagnetic-phase region and the XY1-phase region, only when $J_{1,b} \gtrsim 1.2$. It shows further that the phase transition between the ferromagnetic and partial ferrimagnetic phases is between the $M_g(L) = L$ and $M_g(L) = L - 1$ states, while that between the partial ferrimagnetic and XY1 phases is between the $M_g(L) = 1$ and $M_g(L) = 0$ states or between the $L - 1 \geq M_g(L) \geq 2$ and $M_g(L) = 0$ states depending upon whether $J_{1,b} \gtrsim 1.55$ or $1.55 \gtrsim J_{1,b} \gtrsim 1.2$. Thus, it may be considered that the former transition is always of the second-order, while the latter transition is of the second-order when $J_{1,b} \gtrsim 1.55$ and of the first-order when $1.55 \gtrsim J_{1,b} \gtrsim 1.2$. The Δ_1 -dependences of $M_g(L)$'s for $L = 6$,

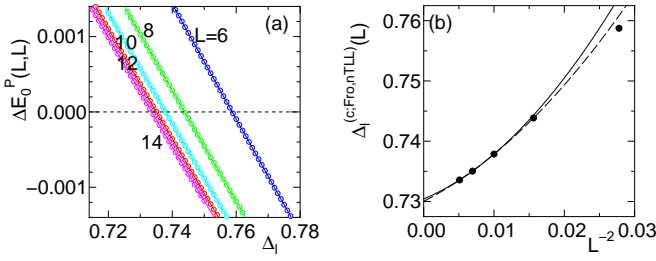


Fig. 6. (Color online) (a) Plot of $\Delta E_0^{\text{P}}(L, L)$ versus Δ_1 for $J_{1,b} = -0.7$. The correspondence of the color of each line to the value of each L is the same as that in Fig. 3(a). (b) Plot of $\Delta_1^{(\text{c}; \text{Fro, nTLL})}(L)$ versus L^{-2} for $J_{1,b} = -0.7$. The meanings of the solid and dashed lines are the same as those in Fig. 3(b). The extrapolated value to $L \rightarrow \infty$ is given by $\Delta_1^{(\text{c}; \text{Fro, nTLL})} = 0.730 \pm 0.001$.

8, \dots , 14 in the cases of $J_{1,b} = 2.0$ and 1.3 are depicted in Figs. 7(a) and (b), respectively. The phase boundary line between the ferromagnetic and partial ferrimagnetic phases can be analytically calculated by examining the instability of the one-magnon excitation from the ferromagnetic state. However, since this calculation is straightforward but too tedious, we show in Fig. 2 the numerical result obtained by solving

$$\Delta E_0^{\text{P}}(L, L) = \Delta E_0^{\text{P}}(L, L-1). \quad (9)$$

It is noted that the obtained finite-size critical value is independent of L (the magenta line). This means that in the present case, the $M_g(L) = L-1$ state with the lowest energy is a commensurate state. The finite-size critical value $\Delta_1^{(\text{c}; \text{PFri, XY1})}(L)$ of Δ_1 , for a given value of $J_{1,b}$, for the second-order phase transition between the partial ferrimagnetic and XY1 phases is calculated by solving

$$\Delta E_0^{\text{P}}(L, 1) = 0. \quad (10)$$

Figure 8 illustrates the determination of the corresponding critical value $\Delta_1^{(\text{c}; \text{PFri, XY1})}$ at the thermodynamic limit in the case where $J_{1,b} = 2.0$ (the red line). Generally speaking, it is difficult to accurately determine the critical value $\Delta_1^{(\text{c}; \text{PFri, XY1})}$ of Δ_1 at the thermodynamic limit, for a given value of $J_{1,b}$, for the first-order phase transition between the partial ferrimagnetic and XY1 phases by performing only the ED calculations for finite- L systems with up to $L = 14$ rungs. Fortunately, however, in the present case the corresponding finite-size critical value $\Delta_1^{(\text{c}; \text{PFri, XY1})}(L)$ of Δ_1 is almost independent of L , as can be seen from Fig. 7(b), and therefore we use $\Delta_1^{(\text{c}; \text{PFri, XY1})}(14)$ for $\Delta_1^{(\text{c}; \text{PFri, XY1})}$ (the black line). We consider that the numerical error due to this simplification is less than 0.001.

Lastly (the cyan line in Fig. 2), the phase transition between the Haldane and Néel phases is the 2D Ising-type transition. In this case, the critical value $\Delta_1^{(\text{c}; \text{H, N})}$ of Δ_1 at the thermodynamic limit for a given value of $J_{1,b}$ can be evaluated by the phenomenological renormalization-group (PRG) method³⁷⁾ in the following way. We cal-

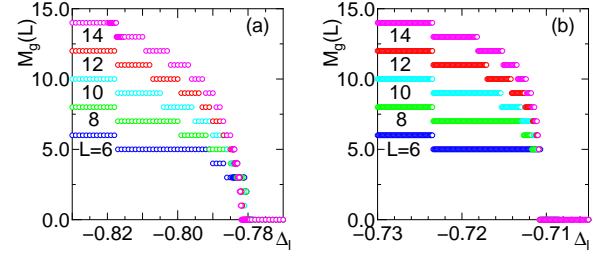


Fig. 7. (Color online) Plot of $M_g(L)$ versus Δ_1 in the cases of (a) $J_{1,b} = 2.0$ and (b) $J_{1,b} = 1.3$. The correspondence of the color of each line to the value of each L is the same as that in Fig. 3(a).

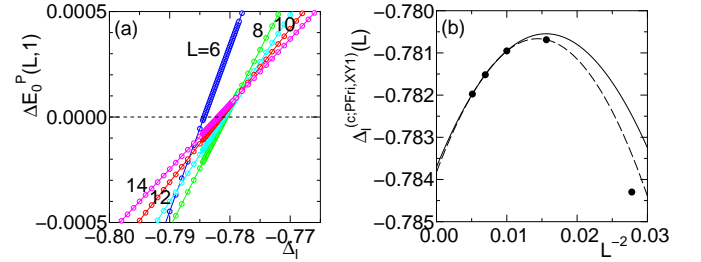


Fig. 8. (Color online) (a) Plot of $\Delta E_0^{\text{P}}(L, 1)$ versus Δ_1 for $J_{1,b} = 2.0$. The correspondence of the color of each line to the value of each L is the same as that in Fig. 3(a). (b) Plot of $\Delta_1^{(\text{c}; \text{PFri, XY1})}(L)$ versus L^{-2} for $J_{1,b} = 2.0$. The meanings of the solid and dashed lines are the same as those in Fig. 3(b). The extrapolated value to $L \rightarrow \infty$ is given by $\Delta_1^{(\text{c}; \text{PFri, XY1})} = -0.784 \pm 0.001$.

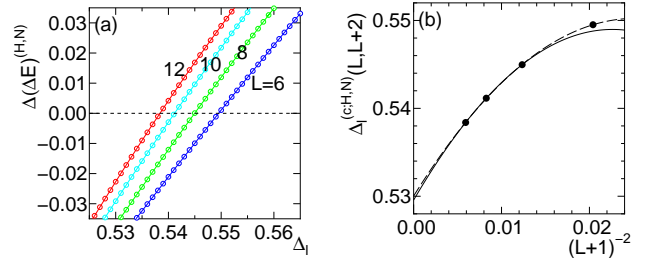


Fig. 9. (Color online) (a) Plot of $\Delta(\Delta E)^{(\text{H, N})} [\equiv L \Delta E_1^{\text{P}}(L, 0) - (L+2) \Delta E_1^{\text{P}}(L+2, 0)]$ versus Δ_1 for $J_{1,b} = 2.0$. The correspondence of the color of each line to the value of each L is the same as that in Fig. 3(a). (b) Plot of $\Delta_1^{(\text{c}; \text{H, N})}(L, L+2)$ versus $(L+1)^{-2}$ for $J_{1,b} = 2.0$. The solid and dashed lines represent, respectively, the least-squares fittings where the data from $L = 8$ to $L = 12$ and the data from $L = 6$ to $L = 12$ are used. The extrapolated value to $L \rightarrow \infty$ is given by $\Delta_1^{(\text{c}; \text{H, N})} = 0.530 \pm 0.001$.

culate the finite-size critical value $\Delta_1^{(\text{c}; \text{H, N})}(L, L+2)$ by solving the PRG equation given by

$$L \Delta E_1^{\text{P}}(L, 0) = (L+2) \Delta E_1^{\text{P}}(L+2, 0). \quad (11)$$

Then, we extrapolate the finite-size results to the $L \rightarrow \infty$ limit to evaluate $\Delta_1^{(\text{c}; \text{H, N})}$. In a practical extrapolation we fitted them to a quadratic function of $(L+1)^{-2}$ by using the least-squares method. In Fig. 9 we illustrate this procedure for the case of $J_{1,b} = 2.0$.

Before closing this section, we make two more comments on the phase diagram shown in Fig. 2. First, there are two tetracritical points, at one of which the ferromagnetic-nematic TLL and Néel-nematic TLL phase boundary lines come in contact with each other, and at the other the XY1-Haldane, Haldane-Néel, Néel-nematic TLL, and nematic TLL-XY1 phase boundary lines merge. As regards the latter tetracritical point, we have concluded that this is the case based on the physical consideration by referring to the result of the perturbational calculation discussed in Sect. 3 [see Fig. 10(b)]. We note that it is hard to draw this conclusion only from the present ED calculation for finite- L systems with up to $L=14$ rungs. Secondly, the results of our ED calculation suggest that, when the value of $J_{1,b}$ is sufficiently small (at least when $J_{1,b} \lesssim -4.0$), the XY1 phase may appear below the Néel phase. The phase transition between these two phases is the BKT transition with the STSB, and the phase boundary line can be estimated from the equation^{3,5,6)}

$$\Delta E_1^P(L, 0) = \Delta E_0^P(L, 1) \quad (12)$$

instead of Eq. (5). We have tried to estimate this phase boundary line in a similar way. Although the finite-size critical points which satisfy Eq. (12) exist, the numerical error coming from the extrapolation $L \rightarrow \infty$ is fairly large in this case. Thus, we believe that the XY1 phase exists in this region, but it is difficult to draw the phase boundary line. In order to overcome this difficulty, it is indispensable to attempt more sophisticated analyses, which are beyond the scope of the present study.

3. Perturbational Calculations

In order to elucidate the characteristic features of the phase diagram shown in Fig. 2, we have performed the first-order perturbational calculation from the strong-rung coupling limit. We begin with the two-spin problem of the j th rung;

$$\mathcal{H}_r = J_r \left\{ \Gamma_r \left(S_{j,a}^x S_{j,b}^x + S_{j,a}^y S_{j,b}^y \right) + S_{j,a}^z S_{j,b}^z \right\}. \quad (13)$$

The eigenstates and the eigenenergies of \mathcal{H}_r are as follows:

$$|\psi_1\rangle = |\uparrow_{j,a}\uparrow_{j,b}\rangle, \quad E_1 = \frac{J_r}{4}, \quad (14)$$

$$|\psi_2\rangle = \frac{|\uparrow_{j,a}\downarrow_{j,b}\rangle + |\downarrow_{j,a}\uparrow_{j,b}\rangle}{\sqrt{2}}, \quad E_2 = \frac{J_r(2\Gamma_r - 1)}{4}, \quad (15)$$

$$|\psi_3\rangle = |\downarrow_{j,a}\downarrow_{j,b}\rangle, \quad E_3 = \frac{J_r}{4}, \quad (16)$$

$$|\psi_4\rangle = \frac{|\uparrow_{j,a}\downarrow_{j,b}\rangle - |\downarrow_{j,a}\uparrow_{j,b}\rangle}{\sqrt{2}}, \quad E_4 = -\frac{J_r(2\Gamma_r + 1)}{4}, \quad (17)$$

where $|\uparrow_{j,\ell}\rangle$ and $|\downarrow_{j,\ell}\rangle$ denote, respectively, the $S_{j,\ell}^z = \frac{1}{2}$ and $S_{j,\ell}^z = -\frac{1}{2}$ states. We take first the three states $|\psi_1\rangle$, $|\psi_2\rangle$, and $|\psi_3\rangle$, and neglect the $|\psi_4\rangle$ state, because we suppose that $J_r (= -1)$ is ferromagnetic. In this restricted space, we interpret these three states as being the $T_j^z = +1$, $T_j^z = 0$, and $T_j^z = -1$ states, respectively, of

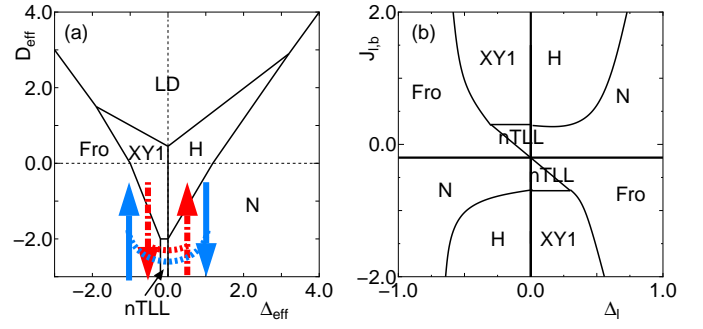


Fig. 10. (Color online) (a) Schematic phase diagram of \mathcal{H}_{eff} numerically obtained by Chen *et al.*⁹⁾ The regions designated by LD, Fro, XY1, H, N, and nTLL are those of the large- D , ferromagnetic, XY1, Haldane, Néel, and nematic TLL phases, respectively. (b) Schematic phase diagram of the present system (\mathcal{H}) predicted by the perturbation theory based on \mathcal{H}_{eff} in the same case ($J_{1,a}=0.2$, $J_r=-1.0$, and $\Gamma_r=0.5$) as that in Fig. 2.

the pseudospin operator \vec{T}_j with $T_j=1$. Comparing the matrix elements, we see that the original spin operators $S_{j,\ell}^\mu$ ($\mu=x,y,z$) can be expressed by

$$S_{j,\ell}^\mu = \frac{1}{2} T_j^\mu \quad (18)$$

within the restricted space. Thus, in the first-order perturbation theory, we can obtain the effective Hamiltonian

$$\mathcal{H}_{\text{eff}} = J_{\text{eff}} \left\{ \sum_{j=1}^L (T_j^x T_{j+1}^x + T_j^y T_{j+1}^y + \Delta_{\text{eff}} T_j^z T_{j+1}^z) + D_{\text{eff}} \sum_{j=1}^L (T_j^z)^2 \right\}, \quad (19)$$

$$J_{\text{eff}} = \frac{J_{1,a} + J_{1,b}}{4}, \quad (20)$$

$$\Delta_{\text{eff}} = \Delta_1, \quad (21)$$

$$D_{\text{eff}} = \frac{J_r(1 - \Gamma_r)}{2J_{\text{eff}}}, \quad (22)$$

where the D_{eff} term comes from the energy differences $E_1 - E_2$ and $E_3 - E_2$. The effective Hamiltonian (19) is a fundamental model for the anisotropic $T=1$ chain, which has been investigated by several authors.⁷⁻⁹⁾ In particular, Chen *et al.*⁹⁾ have numerically determined the phase diagram of \mathcal{H}_{eff} on the Δ_{eff} versus D_{eff} plane.

Figure 10(a) schematically shows the above-mentioned phase diagram of the effective Hamiltonian \mathcal{H}_{eff} obtained by Chen *et al.*⁹⁾ We have chosen that $J_{1,a}=0.2$, $J_r=-1.0$, and $\Gamma_r=0.5$, and therefore the parameters in \mathcal{H}_{eff} are given by

$$J_{\text{eff}} = \frac{J_{1,b} + 0.2}{2}, \quad (23)$$

$$\Delta_{\text{eff}} = \Delta_1, \quad (24)$$

$$D_{\text{eff}} = -\frac{1}{J_{1,b} + 0.2}. \quad (25)$$

From Fig. 10(a), \mathcal{H}_{eff} , and the above three equations, we

obtain the phase diagram given in Fig. 10(b). This phase diagram has a point symmetry with respect to the point $(\Delta_1, J_{1,b}) = (0.0, -0.2)$, which can be explained as follows. If we make the unitary transformations,

$$T_{2j}^x \rightarrow -T_{2j}^x, \quad T_{2j}^y \rightarrow -T_{2j}^y, \quad T_{2j}^z \rightarrow T_{2j}^z, \quad (26)$$

$$T_{2j+1}^x \rightarrow T_{2j+1}^x, \quad T_{2j+1}^y \rightarrow T_{2j+1}^y, \quad T_{2j+1}^z \rightarrow T_{2j+1}^z, \quad (27)$$

the effective Hamiltonian \mathcal{H}_{eff} is transformed into

$$\mathcal{H}_{\text{eff}} \rightarrow -J_{\text{eff}} \left\{ \sum_{j=1}^L (T_j^x T_{j+1}^x + T_j^y T_{j+1}^y - \Delta_{\text{eff}} T_j^z T_{j+1}^z) - D_{\text{eff}} \sum_{j=1}^L (T_j^z)^2 \right\}. \quad (28)$$

Thus, we see that the two points, $(J_{\text{eff}}, \Delta_{\text{eff}}, D_{\text{eff}})$ and $(-J_{\text{eff}}, -\Delta_{\text{eff}}, -D_{\text{eff}})$, belong to the same phase. The transformation

$$(J_{\text{eff}}, \Delta_{\text{eff}}, D_{\text{eff}}) \rightarrow (-J_{\text{eff}}, -\Delta_{\text{eff}}, -D_{\text{eff}}) \quad (29)$$

can be carried out by

$$J_{1,b} + 0.2 \rightarrow -(J_{1,b} + 0.2), \quad (30)$$

$$\Delta_1 \rightarrow -\Delta_1, \quad (31)$$

which explains the point symmetry of the phase diagram shown in Fig. 10(b).

The above arguments concerning the point symmetry will explain the reason why the ferromagnetic, Néel, and nematic TLL phases appear in two places in Fig. 2(a). They suggest that the XY1 state appears as the ground state on the lower outside of Fig. 2(a) ($J_{1,b} < -2.0$). Although we believe the existence of the XY1 phase, we are unfortunately not able to determine its phase boundary, as already noted in the last paragraph in Sect. 2. Also, the Haldane phase does not appear in the region of negative $J_{1,b}$ in Fig. 2(a), and further the partial ferrimagnetic phase found in Fig. 2(a) does not appear in Fig. 10(a). We think that the appearance of the partial ferrimagnetic phase is attributed to the strong frustration effect, which is not taken into account in the present first-order perturbational calculation.

Let us explain the correspondence between Fig. 2(a) and Fig. 10(a) a little bit more in detail. When $J_{1,b}$ changes, on the vertical line $\Delta_1 = 1.0$ in Fig. 2(a), from a large positive value to -0.2 , the parameter J_{eff} is always positive, $\Delta_{\text{eff}} = 1.0$, and D_{eff} changes from a small negative value to a large negative value. Thus, the corresponding point in Fig. 10(a) moves along the downward-arrowed blue solid line. On the other hand, when $J_{1,b}$ changes, again on the vertical line $\Delta_1 = 1.0$ in Fig. 2(a), from -0.2 to a large negative value, the parameter J_{eff} is always negative, $\Delta_{\text{eff}} = 1.0$, and D_{eff} changes from a large positive value to a small positive value. Since the points $(J_{\text{eff}}, \Delta_{\text{eff}}, D_{\text{eff}})$ and $(-J_{\text{eff}}, -\Delta_{\text{eff}}, -D_{\text{eff}})$ belong to the same phase as already explained, these changes in the parameters in \mathcal{H}_{eff} are equivalent to those in the case where J_{eff} is positive, $\Delta_{\text{eff}} = -1.0$, and D_{eff} changes

from a large negative value to a small negative value. Namely, the corresponding point in Fig. 10(a) moves along the upward-arrowed blue solid line. Although the two blue solid lines are separated from each other, we surmise that they are connected with each other by the blue dotted line in the higher-order perturbation theory at least near $\Delta_{\text{eff}} = 0.0$. Another possibility is that they are connected through $\Delta_{\text{eff}} = \pm\infty$. Thus, the phase of the original system \mathcal{H} successively changes to the Néel, nematic TLL, and ferromagnetic phases with decreasing $J_{1,b}$, which well explains the phases on the $\Delta_1 = 1.0$ line in Fig. 2(a). We can make a very similar discussion, for example, for the line $\Delta_1 = -0.5$ in Fig. 2(a) by use of the red dot-dashed lines in Fig. 10(a). Namely, the phase successively changes to the XY1, ferromagnetic, nematic TLL, and Néel phases with decreasing $J_{1,b}$ in this case. Thus, the perturbational calculation together with the numerical result obtained by Chen *et al.*⁹⁾ qualitatively explains the numerically determined phase diagram of the present system (\mathcal{H}).

Here, we discuss the validity of the perturbational calculation. At a glance, this perturbational calculation is thought to be valid for the strong-rung coupling case, $|J_{1,b}| \ll |J_r|$. However, the bosonization theory from the weak-rung coupling limit shows that the rung coupling is relevant and is renormalized to the strong-rung coupling case, as is known in the simple ladder case. This fact strongly suggests that the present perturbational calculation is qualitatively valid even for the weak-rung coupling case.

4. DMRG Calculations

In this section, we present several results of the DMRG calculation, which supplement the reliability of the phase diagram shown in Fig. 2. In this calculation, we assume the open boundary condition (OBC) for the Hamiltonian \mathcal{H} , where the sum over j is taken from $j=1$ to $j=L-1$. We treat the finite-size systems with up to $L=96$ rungs, L being assumed to be even. The number of block states in the DMRG calculation required to achieve the desired accuracy depends on the state targeted. In our calculation, we have kept up to 600 block states for the most severe case and checked that the results are accurate enough for our arguments below by monitoring the dependences of the data and the truncation error on the number of kept states.

The physical quantities which we calculate and analyze are the energy gaps $\Delta E^{\text{O}}(L, 1)$ and $\Delta E^{\text{O}}(L, 2)$, the local magnetization $m_\ell^{\text{O}}(j; L, M)$, the two-spin correlation function $\omega_\ell^{\mu\mu, \text{O}}(j; L, M)$ ($\mu = x, z$), and the nematic four-spin correlation function $\omega_\ell^{+-+-, \text{O}}(j; L, M)$. Among these quantities, $\Delta E^{\text{O}}(L, 1)$ and $\Delta E^{\text{O}}(L, 2)$ are defined, respectively, by

$$\Delta E^{\text{O}}(L, 1) = E_0^{\text{O}}(L, 1) - E_0^{\text{O}}(L, 0), \quad (32)$$

$$\Delta E^{\text{O}}(L, 2) = E_0^{\text{O}}(L, 2) - E_0^{\text{O}}(L, 0), \quad (33)$$

where $E_0^{\text{O}}(L, M)$ is the lowest-energy eigenvalue of \mathcal{H} under the OBC within the subspace determined by L and M . It is noted that except for the ferromagnetic and

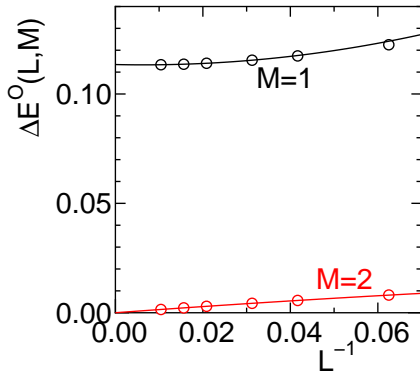


Fig. 11. (Color online) Dependences of $\Delta E^O(L,1)$ and $\Delta E^O(L,2)$ on L^{-1} at the point ($\Delta_1=0.5, J_{1,b}=-0.5$) (in the nematic TLL phase) in the phase diagram shown in Fig. 2. The solid lines represent the least-squares fittings, where the data for $L=32, 48, 64, 96$ are used.

partial ferrimagnetic phases, $E_0^O(L,0)$ gives the ground-state energy. Further, $m_\ell^O(j; L, M)$ is defined by

$$m_\ell^O(j; L, M) = \langle S_{j,\ell}^z \rangle_{L,M}, \quad (34)$$

and also $\omega_\ell^{\mu\mu,0}(j; L, M)$ and $\omega_\ell^{+-+-,0}(j; L, M)$ are defined, respectively, by

$$\omega_\ell^{\mu\mu,0}(j; L, M) = \langle S_{j_0,\ell}^\mu S_{j_0+j,\ell}^\mu \rangle_{L,M}, \quad (35)$$

$$\omega^{+-+-,0}(j; L, M) = \langle S_{j_0,a}^+ S_{j_0,b}^+ S_{j_0+j,a}^- S_{j_0+j,b}^- \rangle_{L,M}, \quad (36)$$

where depending upon whether $j(>0)$ is odd or even, $j_0 = \frac{L+1-j}{2}$ or $j_0 = \frac{L-j}{2}$, respectively, which means that the two rungs j_0 and j_0+j are at (almost) equal distances from the center of the open ladder. In the above three equations, $\langle \dots \rangle_{L,M}$ denotes the expectation value associated with the lowest-energy state within the subspace determined by L and M in the system under the OBC; when $M=M_g(L)$, this expectation value is simply the ground-state expectation value for the system with L rungs.

Figure 11 shows our DMRG results for the $1/L$ -dependence of the energy gaps $\Delta E^O(L,1)$ and $\Delta E^O(L,2)$ at the point ($\Delta_1=0.5, J_{1,b}=-0.5$), which belongs to the nematic-TLL-phase region in the phase diagram shown in Fig. 2. Performing the $L \rightarrow \infty$ extrapolation of these gaps, $\Delta E^O(L, M)$'s, we have fitted them to quadratic functions of L^{-1} by use of the least-squares method. The solid lines in Fig. 11, which show these extrapolations, demonstrate that at the thermodynamic ($L \rightarrow \infty$) limit, the former gap is finite [$\Delta E^O(1) \sim 0.113$], while the latter gap vanishes [$\Delta E^O(2) \sim 6 \times 10^{-6}$]. The binding energy of two magnons is given by $E_{\text{betm}} = 2\Delta E^O(1) - \Delta E^O(2) \sim 0.227$ and is definitely finite, which is consistent with the fact that the nematic TLL state accompanies the two-magnon bound state. In Fig. 12 we present the DMRG results for the correlation functions for $L=96$ and $M=0$ at the point ($\Delta_1=0.5, J_{1,b}=-0.5$). We note that the four-rung-period oscillation as a function of j in the correlation func-

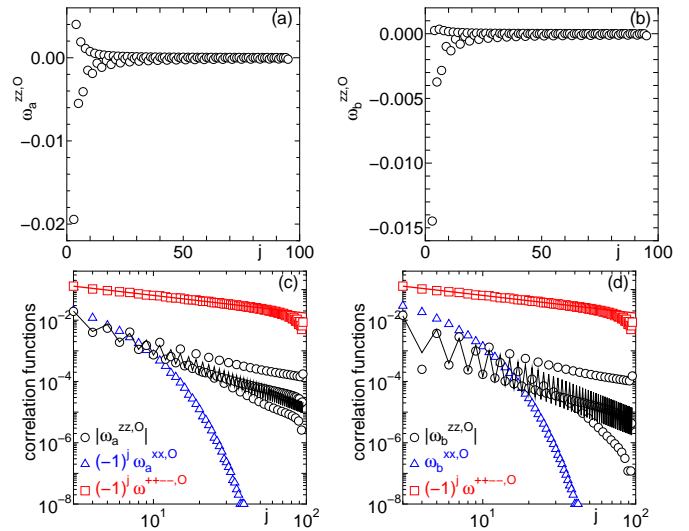


Fig. 12. (Color online) Correlation functions at the point ($\Delta_1=0.5, J_{1,b}=-0.5$) (in the nematic TLL phase). In (a) and (b), the j -dependences of $\omega_\ell^{zz,0}(j; 96, 0)$ for $\ell=a$ and $\ell=b$, respectively, are shown in a linear scale. In (c), $|\omega_a^{zz,0}(j; 96, 0)|$, $(-1)^j \omega_a^{xx,0}(j; 96, 0)$, and $(-1)^j \omega^{+-+-,0}(j; 96, 0)$ are shown in a log-log scale, while in (d), $|\omega_b^{zz,0}(j; 96, 0)|$, $\omega_b^{xx,0}(j; 96, 0)$, and $(-1)^j \omega^{+-+-,0}(j; 96, 0)$ are shown in a log-log scale. [Note that the same data of $(-1)^j \omega^{+-+-,0}(j; 96, 0)$ are shown in both (c) and (d) for comparison.] The solid lines in (c) and (d) represent the least-squares fitting of $\omega_\ell^{zz,0}(j; 96, 0)$ and $\omega^{+-+-,0}(j; 96, 0)$ to Eqs. (37) and (38), respectively, where the data from $j=6$ to $j=36$ are used.

tion $\omega_\ell^{zz,0}(j; 96, 0)$ comes from the open boundary effect.³⁸⁾ From the figure, we see that the transverse two-spin correlation function $\omega_\ell^{xx,0}(j; 96, 0)$ decays exponentially, while the longitudinal two-spin correlation function $\omega_\ell^{zz,0}(j; 96, 0)$ and the nematic four-spin correlation function $\omega^{+-+-,0}(j; 96, 0)$ decay algebraically. Here, as is expected, $\omega^{+-+-,0}(j; 96, 0)$ is more dominant than $\omega_\ell^{zz,0}(j; 96, 0)$. The asymptotic forms of the latter two correlation functions in the nematic TLL phase are expected to be³⁹⁾

$$\omega_\ell^{zz,0}(j; L \rightarrow \infty, 0) \sim (-1)^j \frac{\alpha_{1,\ell}}{j \eta_\ell^{zz}} + \frac{\alpha_{2,\ell}}{j^2}, \quad (37)$$

$$\omega^{+-+-,0}(j; L \rightarrow \infty, 0) \sim (-1)^j \frac{\alpha}{j \eta^{+-+-}}, \quad (38)$$

where $\alpha_{1,\ell}$, $\alpha_{2,\ell}$, and α are numerical constants. The decay exponents obey the relation $\eta_\ell^{zz} \eta^{+-+-} = 1$. We have performed the least-squares fitting of the nematic four-spin correlation function $\omega^{+-+-,0}(j; 96, 0)$ to Eq. (38) using the data for $6 \leq j \leq 36$. We have thereby obtained the estimate of the decay exponent, $\eta^{+-+-} \sim 0.577$, which is much smaller than 1 and supports the prediction of the dominant nematic correlation. For the longitudinal two-spin correlations, we have unfortunately not been able to achieve a precise estimation of the decay exponent due to rather large open-boundary effects. We have fitted $\omega_\ell^{zz,0}(j; 96, 0)$ to Eq. (37) using the data for several ranges of j , namely, $3 \leq j \leq 20$, $4 \leq j \leq 24$, $5 \leq j \leq 30$, and $6 \leq j \leq 36$. Then, we have obtained the estimates

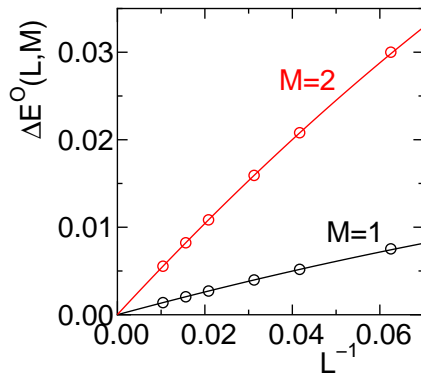


Fig. 13. (Color online) Dependences of $\Delta E^O(L,1)$ and $\Delta E^O(L,2)$ on L^{-1} at the point ($\Delta_1 = -0.25, J_{1,b} = 1.0$) (in the XY1 phase) in the phase diagram shown in Fig. 2. The solid lines represent the least-squares fittings, where the data for $L = 32, 48, 64, 96$ are used.

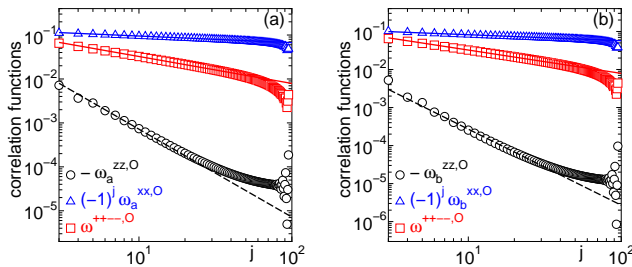


Fig. 14. (Color online) Correlation functions at the point ($\Delta_1 = -0.25, J_{1,b} = 1.0$) (in the XY1 phase). In (a) and (b), $-\omega_\ell^{zz,O}(j; 96, 0)$ and $(-1)^j \omega_\ell^{xx,O}(j; 96, 0)$ for $\ell = a$ and $\ell = b$, respectively, are shown in a log-log scale, while $\omega^{+ + - -,O}(j; 96, 0)$ is shown in both (a) and (b) for comparison. The solid lines represent the least-squares fittings of $\omega_\ell^{xx,O}(j; 96, 0)$ and $\omega^{+ + - -,O}(j; 96, 0)$ to Eqs. (39) and (40), respectively, where the data from $j = 6$ to $j = 36$ are used. The dashed lines show the power-law decay behavior, $\sim 1/j^2$, of $\omega_\ell^{zz,O}(j; 96, 0)$, where the first term in Eq. (37) is neglected.

in the ranges of $1.70 \leq \eta_a^{zz} \leq 2.11$ and $1.63 \leq \eta_b^{zz} \leq 2.31$. Although these estimates show rather large variations, the values are consistent with the expectation $\eta_\ell^{zz} = 1/\eta^{+ + - -}$, namely, $\eta_\ell^{zz} \sim 1/0.577 = 1.73$, and indicate that the longitudinal spin correlation decays much faster than the nematic correlation. The DMRG data thereby support the result of the ED analysis that the system at the point ($\Delta_1 = 0.5, J_{1,b} = -0.5$) belongs to the nematic TLL phase. It is also emphasized that η_a^{zz} and η_b^{zz} are almost equal to each other in spite of the fact that $J_{1,a}$ is positive, while $J_{1,b}$ is negative. This result reflects the fact that the nematic TLL is a one-component TLL,^{11,12} which leads to the same decay exponents of the correlation functions within the a leg and within the b leg.

Figure 13 displays the $1/L$ -dependences of the energy gaps $\Delta E^O(L,1)$ and $\Delta E^O(L,2)$ at the point ($\Delta_1 = -0.25, J_{1,b} = 1.0$), which belongs to the XY1-phase region in the phase diagram shown in Fig. 2. We have estimated the limiting ($L \rightarrow \infty$) values of these energy gaps in the same way as that in the case of the point ($\Delta_1 = 0.5,$

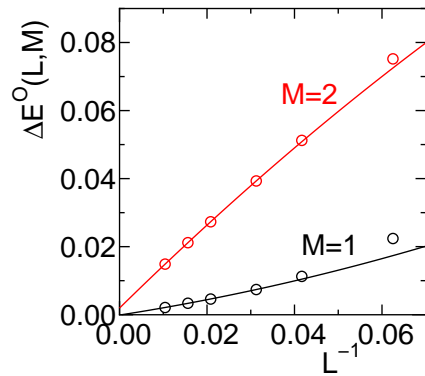


Fig. 15. (Color online) Dependences of $\Delta E^O(L,1)$ and $\Delta E^O(L,2)$ on L^{-1} at the point ($\Delta_1 = 0.25, J_{1,b} = 1.0$) (in the Haldane phase) in the phase diagram shown in Fig. 2. The solid lines represent the least-squares fittings where the data for $L = 32, 48, 64, 96$ are used.

$J_{1,b} = -0.5$) (see the solid lines in Fig. 13), and obtained the results that both gaps vanish [$\Delta E^O(1) \sim 5 \times 10^{-6}$ and $\Delta E^O(2) \sim 2 \times 10^{-5}$]. The DMRG results for the correlation functions for $L = 96$ and $M = 0$ at the point ($\Delta_1 = -0.25, J_{1,b} = 1.0$) are depicted in Fig. 14. In this case, all of the three correlation functions decay algebraically. It is expected³⁹ that the asymptotic form of $\omega_\ell^{zz,O}(j; L \rightarrow \infty, 0)$ in the XY1 phase is again given by Eq. (37), while those of $\omega_\ell^{xx,O}(j; L \rightarrow \infty, 0)$ and $\omega^{+ + - -,O}(j; L \rightarrow \infty, 0)$ in this phase are written as

$$\omega_\ell^{xx,O}(j; L \rightarrow \infty, 0) \sim (-1)^j \frac{\alpha'_\ell}{j \eta_\ell^{xx}}, \quad (39)$$

$$\omega^{+ + - -,O}(j; L \rightarrow \infty, 0) \sim \frac{\alpha'}{j \eta^{+ + - -}}, \quad (40)$$

where α'_ℓ and α' are constants. It is also expected that the longitudinal and transverse spin correlations are dual to each other, resulting in the relation $\eta_\ell^{xx} \eta_\ell^{zz} = 1$, while the exponent of the nematic correlation function is related to that of the transverse-spin correlation function as $\eta^{+ + - -} = 4\eta_\ell^{xx}$. We have estimated η_ℓ^{xx} and $\eta^{+ + - -}$ by the least-squares fitting of $\omega_\ell^{xx,O}(j; 96, 0)$ and $\omega^{+ + - -,O}(j; 96, 0)$ to Eqs. (39) and (40), respectively, using the numerical data for $6 \leq j \leq 36$. The results are $\eta_a^{xx} \sim 0.15$, $\eta_b^{xx} \sim 0.16$, and $\eta^{+ + - -} \sim 0.61$, which support the expectation that $\eta^{+ + - -} = 4\eta_\ell^{xx}$. For the longitudinal-spin correlation function, we have found that $\omega_\ell^{zz,O}(j; 96, 0)$ is negative for all j and that the oscillating component is far from sizable, indicating that the second (uniform) term in Eq. (37) is much more dominant than the first (oscillating) term. This observation, with our estimate $\eta_\ell^{xx} \sim 0.15-0.16$ above, is found to be consistent with the expectation that $\eta_\ell^{xx} \eta_\ell^{zz} = 1$, since $\eta_\ell^{zz} = 1/\eta_\ell^{xx} \sim 6.3-6.7$ is much larger than 2, the exponent of the uniform component.

Figure 15 shows the $1/L$ -dependences of the energy gaps $\Delta E^O(L,1)$ and $\Delta E^O(L,2)$ at the point ($\Delta_1 = 0.25, J_{1,b} = 1.0$), which belongs to the Haldane-phase region in the phase diagram shown in Fig. 2. The estimations of the limiting ($L \rightarrow \infty$) values of these en-

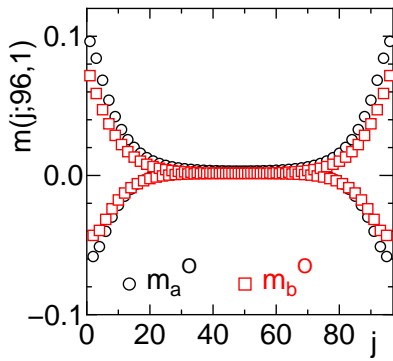


Fig. 16. (Color online) Dependence of $m_\ell^O(j; 96, 1)$ on j at the point $(\Delta_1=0.25, J_{1,b}=1.0)$ (in the Haldane phase).

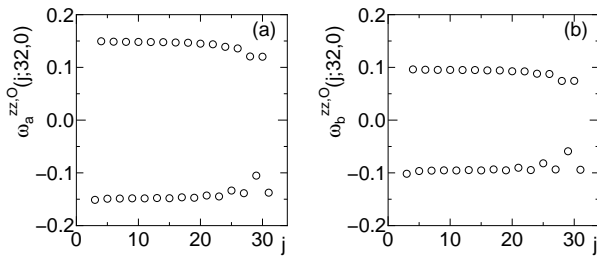


Fig. 17. Dependences of (a) $\omega_a^{zz,O}(j; 32, 0)$ and (b) $\omega_b^{zz,O}(j; 32, 0)$ at the point $(\Delta_1=-0.5, J_{1,b}=-1.0)$ (in the Néel phase) in the phase diagram shown in Fig. 2.

ergy gaps have been performed again in the same way as that in the case of the point $(\Delta_1=0.5, J_{1,b}=-0.5)$ (see the solid lines in Fig. 15). Then, we have obtained the result that the former gap vanishes [$\Delta E^O(1)$ is even negative to be $\sim -9 \times 10^{-5}$]. For the latter gap, we have obtained the extrapolated value $\Delta E^O(2) \sim 0.002$, which is quite small but seems to be finite. These results indicate that the system exhibits a small but nonzero Haldane gap. [Note that in the large ($L \rightarrow \infty$) system under the OBC, the lowest-energy states in the subspace of $M=0$ and 1 are degenerate, and $\Delta E^O(2)$ gives the excitation gap above the degenerate ground states.] The local magnetizations $m_\ell^O(j; L, M)$ for $L=96$ and $M=1$ at the point $(\Delta_1=0.25, J_{1,b}=1.0)$ are plotted as functions of j in Fig. 16. This figure clearly demonstrates that the edge-localized spins appear, which is one of the most distinguishing features of the Haldane state in the $S=1$ chain. All of these results are consistent with the conclusion of the ED analysis that the system at the parameter point $(\Delta_1=0.25, J_{1,b}=1.0)$ is in the Haldane state with a small excitation gap. On the other hand, our DMRG results for the correlation functions in the system with $L=96$, which are not shown here, are unfortunately not able to determine their asymptotic behaviors due to the strong open-boundary effect coming from the large correlation length.

Finally, we depict in Fig. 17 the j -dependences of the correlation functions $\omega_a^{zz,O}(j; L, M)$ and $\omega_b^{zz,O}(j; L, M)$ for $L=32^{40}$ and $M=0$ at the point $(\Delta_1=-0.5, J_{1,b}=-1.0)$, which belongs to the one of the Néel-phase regions

in the phase diagram shown in Fig. 2. From this figure, we see that the strong Néel long-range order (LRO) certainly exists, supporting our conclusion obtained by the ED analysis that the system at this parameter point indeed belongs to the Néel phase. It is noted that we have also obtained a similar result at the point $(\Delta_1=0.75, J_{1,b}=1.0)$ which belongs to another Néel-phase region.

5. Concluding Remarks

We have numerically determined the ground-state phase diagram on the Δ_1 versus $J_{1,b}$ plane of the $S=1/2$ two-leg ladder with different leg interactions, which is governed by the Hamiltonian \mathcal{H} of Eq. (1), confining ourselves to the case where $J_{1,a}=0.2$, $J_r=-1.0$, and $\Gamma_r=0.5$. The resultant phase diagram, which is presented in Fig. 2, consists of the ferromagnetic, Haldane, Néel, nematic TLL, partial ferrimagnetic, and XY1 phases. In addition, the phase diagram on the Γ_r versus $J_{1,b}$ plane in the case where $J_{1,a}=0.2$, $J_r=-1.0$, and $\Delta_1=1.0$, in which the nematic TLL phase also appears, has been obtained (see Fig. A.1 later). By estimating the phase boundary lines, we have successfully applied the LS^{3,5,6,36}) or PRG³⁷) analysis of the numerical data obtained by the ED method to the transition between two of the Haldane, Néel, nematic TLL, and XY1 phases, while we have compared the energies $E_0^P(L, M)$'s for the transition associated with the ferromagnetic and partial ferrimagnetic phases. In our opinion, one of the significant results of the present work is the fact that the nematic TLL phase appears in the strong-rung unfrustrated region as well as in the strong-rung frustrated region.

We have carried out first-order perturbational calculations from the strong-rung coupling limit, in which the present system (\mathcal{H}) is mapped onto the anisotropic $S=1$ chain system (\mathcal{H}_{eff}), in order to outline the essential features of the phase diagram. Furthermore, performing the DMRG^{32,33}) calculations, we have clarified the following. In the Haldane phase, there is a finite excitation gap (the Haldane gap) above the ground state, and the edge-localized spins appear. In the Néel phase, the magnetic LRO of the Néel type is found. In the nematic TLL phase, the two-magnon bound state characterizes this phase, and the nematic four-spin correlation function with a quasi-LRO is more dominant than the longitudinal two-spin correlation function with a quasi-LRO and the transverse two-spin correlation function with a short-range order. In the XY1 phase, all of the three correlation functions exhibit a quasi-LRO, and among them the transverse two-spin correlation function is most dominant.

The recent result of the bosonization analysis for the present system, attempted by one of the authors (S. C. F.) suggests that the nematic TLL phase also appears in the weak-rung frustrated region. This prediction is highly plausible for the following reason. Let us consider a two-magnon excited state in the system of almost independent chains with $(J_{1,a}, \Delta_1)$ and $(J_{1,b}, \Delta_1)$ coupled via the weak rung interaction (J_r, Γ_r) . We assume that $J_{1,a} > 0.0$, $J_{1,b} < 0.0$, $J_r < 0.0$, $|\Delta_1| < 1.0$, and $0.0 \leq \Gamma_r < 1.0$. The ferromagnetic Ising-like rung interaction favors the

formation of the two-magnon bound state in a rung, as mentioned in Sect. 1. On the other hand, if the one-magnon excitation energies in each chain are different, the leg interactions result in two magnons sitting in the chain with the smaller excitation energy, resulting in a scattered state of two magnons. Therefore, at the level of a crude approximation, one can expect that the two magnons form a bound state when $|J_r|$ is sufficiently larger than the difference between the one-magnon excitation energies in each chain,

$$|\Delta(\Delta E)_{\text{om}}| = |(\Delta E)_{\text{om}}(L; J_{1,a}, \Delta_1) - (\Delta E)_{\text{om}}(L; J_{1,b}, \Delta_1)|, \quad (41)$$

where $(\Delta E)_{\text{om}}(L; J_\ell, \Delta_1)$ is the one-magnon excitation energy in an independent chain with $J_{1,\ell}$ and Δ_1 . The $L \rightarrow \infty$ asymptotic form of the one-magnon excitation energy is obtained from the conformal field theory⁴¹⁾ and the Bethe ansatz^{42,43)} as

$$(\Delta E)_{\text{om}}(L; J_{1,a}, \Delta_1) \sim \frac{\pi}{L} v(J_{1,a}, \Delta_1) \eta(\Delta_1), \quad (42)$$

$$(\Delta E)_{\text{om}}(L; J_{1,b}, \Delta_1) \sim \frac{\pi}{L} v(|J_{1,b}|, -\Delta_1) \eta(-\Delta_1) \quad (43)$$

with

$$v(J, \Delta) = \frac{\pi \sqrt{1 - \Delta^2}}{2 \cos^{-1} \Delta} J, \quad (44)$$

$$\eta(\Delta) = 1 - \frac{1}{\pi} \cos^{-1} \Delta. \quad (45)$$

Note that the chain with $(J_{1,b}, \Delta_1)$ is transformed into the chain with $(|J_{1,b}|, -\Delta_1)$ by the π -rotation around the z axis for every other spin. Thus, solving the equation $|\Delta(\Delta E)_{\text{om}}| = 0$ with Eqs. (42)-(45), we can determine the value $\tilde{\Delta}_1$ of Δ_1 at which the difference in the one-magnon excitation energies vanishes. The result is

$$\tilde{\Delta}_1 = \cos \left(\frac{\pi \sqrt{J_{1,a}/|J_{1,b}|}}{1 + \sqrt{J_{1,a}/|J_{1,b}|}} \right), \quad (46)$$

from which, when $J_{1,a} = 0.2$, for example, $\tilde{\Delta}_1 = 0.0$ for $J_{1,b} = -0.2$ and $\tilde{\Delta}_1 = 0.158$ for $J_{1,b} = -0.3$. We thereby expect that, at least for a parameter region around the line $\Delta_1 = \tilde{\Delta}_1$, the inclusion of weak ferromagnetic, Ising-like rung interactions of J_r leads to the formation of a two-magnon bound state. Here, we should mention that the above argument is not sufficient for one-dimensional systems with strong quantum fluctuations, and more sophisticated approaches such as the weak-coupling renormalization group method are required. We are now investigating the ground-state phase diagram in this weak-rung region, and the results will be reported elsewhere.

Finally, we hope that the present work will stimulate future experimental studies on related subjects, which include the synthesis of a ladder system with different leg interactions.

Acknowledgments

We acknowledge Professor Kiyohide Nomura for useful comments. This work has been partly supported by JSPS KAKENHI Grant Numbers JP15K05198, JP15K05882 (J-Physics), JP16J04731, JP16K05419, JP17H02931,

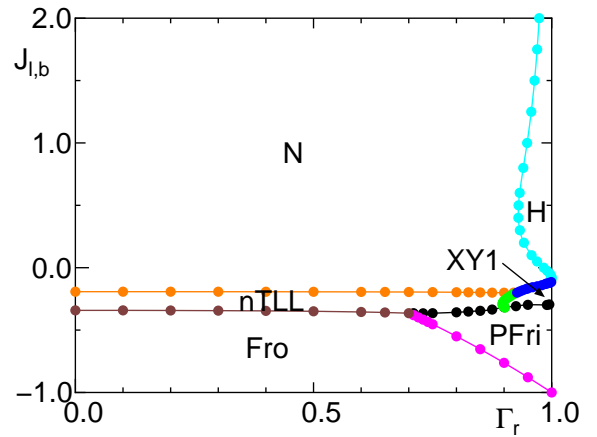


Fig. A.1. (Color online) The ground-state phase diagram on the Γ_r versus $J_{1,b}$ plane in the case where $J_{1,a} = 0.2$, $J_r = -1.0$, and $\Delta_1 = 1.0$, obtained in the present work. The regions designated by N, H, nTLL, XY1, Fro, and PFri are those of the Néel, Haldane, nematic TLL, XY1, ferromagnetic, and partial ferrimagnetic phases, respectively.

and P18H04330 (J-Physics). We also thank the Supercomputer Center, Institute for Solid State Physics, University of Tokyo and the Computer Room, Yukawa Institute for Theoretical Physics, Kyoto University for computational facilities.

Appendix

Figure A.1 demonstrates the obtained ground-state phase diagram on the Γ_r versus $J_{1,b}$ plane in the case where $J_{1,a} = 0.2$, $J_r = -1.0$, and $\Delta_1 = 1.0$. This consists of the Néel, Haldane, nematic TLL, XY1, ferromagnetic, and partial ferrimagnetic phases, all of which are the same as those in Fig. 2. In this phase diagram, the phase boundary line between the Néel and XY1 phases is drawn by the blue line, and the colors of the other lines have the same meanings as those in Fig. 2.

All of the phase boundary lines, except for that for the first-order phase transitions between the partial ferrimagnetic phase and one of the nematic TLL and XY1 phases, have been numerically determined in a way similar to those discussed in Sect. 2; in this case, Okamoto and Nomura's LS method,^{3,5,6)} where we use Eq. (12), works very well for estimating the phase boundary line between the Néel and XY1 phases. Obtaining the phase boundary line for the above first-order phase transitions, we have calculated $M_g(L)$ by carrying out DMRG calculations for the finite system with $L = 36$ rungs under the OBC. We consider that the result for the $L = 36$ system gives a fairly good approximation of the result at the $L \rightarrow \infty$ limit.

The perturbation theory developed in Sect. 3 predicts the phase diagram shown in Fig. A.2 in the following way. Here, the parameter Δ_{eff} is given by $\Delta_{\text{eff}} = 1.0$, since $\Delta_1 = 1.0$. Thus, the $J_{1,b} > -0.2$ and $J_{1,b} < -0.2$ regions in Fig. A.1 correspond, respectively, to the downward- and upward-arrowed blue solid lines in Fig. 10(a). The Haldane-Néel transition point on the $\Delta_{\text{eff}} = 1.0$ line in

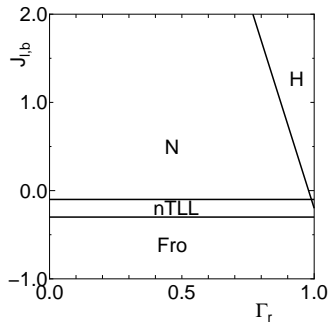


Fig. A.2. Schematic phase diagram of the present system (\mathcal{H}) predicted by the perturbation theory based on \mathcal{H}_{eff} in the same case ($J_{l,a}=0.2$, $J_r=-1.0$, and $\Delta_1=1.0$) as that in Fig. A.1. The regions designated by N, H, nTLL, and Fro are those of the Néel, Haldane, nematic TLL, and ferromagnetic phases, respectively.

Fig. 10(a) can be read as $D_{\text{eff}} \simeq -0.21$, which leads to

$$J_{l,b} = -9.5\Gamma_r + 9.3, \quad (\text{A.1})$$

by using Eqs. (20) and (22). This line well explains the Haldane-Néel boundary line in Fig. A.1 near the point $(\Gamma_r, J_{l,b})=(1.0, 0.0)$, around which the perturbation theory is developed. The crossing of the blue dotted line with the bandlike nematic TLL region in Fig. 10(a) leads to the horizontal nematic TLL band in Fig. A.2. The predicted phase diagram given in Fig. A.2 qualitatively explains the numerical one given in Fig. A.1, although the XY1 and partial ferrimagnetic phases do not appear in Fig. A.2. The appearance of these phases in Fig. A.1 is due to the frustration effect and is beyond the description of the first-order perturbation theory. We note that the existence of the XY1 phase is considered to be an example of the inversion phenomenon concerning the interaction anisotropy^{20–23}) stated in Sect. 1.

- 1) C. K. Majumdar and D. K. Ghosh, *J. Math. Phys.* **10**, 1399 (1969).
- 2) T. Tonegawa and I. Harada, *J. Phys. Soc. Jpn.* **56**, 2153 (1987).
- 3) K. Okamoto and K. Nomura, *Phys. Lett. A* **169**, 433 (1992).
- 4) T. Tonegawa, I. Harada, and M. Kaburagi, *J. Phys. Soc. Jpn.* **61**, 4665 (1992).
- 5) K. Nomura and K. Okamoto, *J. Phys. Soc. Jpn.* **62**, 1123 (1993).
- 6) K. Nomura and K. Okamoto, *J. Phys. A* **27**, 5773 (1994).
- 7) H. J. Schulz, *Phys. Rev. B* **34**, 6372 (1986).
- 8) M. den Nijs and K. Rommelse, *Phys. Rev. B* **40**, 4709 (1989).
- 9) W. Chen, K. Hida, and B. C. Sanctuary, *Phys. Rev. B* **67**, 104401 (2003).
- 10) A. Läuchli, G. Schmid, and S. Trebst, *Phys. Rev. B* **74**, 144426 (2006).
- 11) T. Vekua, A. Honecker, H.-J. Mikeska, and F. Heidrich-Meisner, *Phys. Rev. B* **76**, 174420 (2007).
- 12) T. Hikihara, L. Kecke, T. Momoi, and A. Furusaki, *Phys. Rev. B* **78**, 144404 (2008).
- 13) J. Sudan, A. Lüscher, and A. M. Läuchli, *Phys. Rev. B* **80**, 140402(R) (2009).
- 14) A. Lavarélo, G. Guillaume, and N. Laflorencie, *Phys. Rev. B* **84**, 144407 (2011), and references therein.

- 15) T. Vekua and A. Honecker, *Phys. Rev. B* **73**, 214427 (2006), and references therein.
- 16) F. Michaud, T. Coletta, S. R. Manmana, J.-D. Picon, and F. Mila, *Phys. Rev. B* **81**, 014407 (2010), and references therein.
- 17) G. I. Japaridze and E. Pogosyan, *J. Phys.: Condens. Matter* **18**, 9297 (2006).
- 18) F. Amiri, G. Sun, H.-J. Mikeska, and T. Vekua, *Phys. Rev. B* **92**, 184421 (2015).
- 19) T. Tonegawa, K. Okamoto, T. Hikihara, and T. Sakai, *J. Phys.: Conf. Ser.* **683**, 012039 (2016).
- 20) K. Okamoto and Y. Ichikawa, *J. Phys. Chem. Solids* **63**, 1575 (2002).
- 21) K. Okamoto, *Prog. Theor. Phys. Suppl.* **145**, 208 (2002).
- 22) A. Tokuno and K. Okamoto *J. Phys. Soc. Jpn. Suppl.* **74**, 157 (2005).
- 23) K. Okamoto, *JPS Conf. Proc.* **1**, 012031 (2014).
- 24) H. Yamaguchi, K. Iwase, T. Ono, T. Shimokawa, H. Nakano, Y. Shimura, N. Kase, S. Kittaka, T. Sakakibara, T. Kawakami, and Y. Hosokoshi, *Phys. Rev. Lett.* **110**, 157205 (2013).
- 25) H. Yamaguchi, H. Miyagai, T. Shimokawa, K. Iwase, T. Ono, Y. Kono, N. Kase, K. Araki, S. Kittaka, T. Sakakibara, T. Kawakami, K. Okunishi, and Y. Hosokoshi, *J. Phys. Soc. Jpn.* **83**, 033707 (2014).
- 26) K. Okunishi and T. Tonegawa, *J. Phys. Soc. Jpn.* **72**, 479 (2003).
- 27) T. Hikihara, T. Momoi, A. Furusaki, and H. Kawamura, *Phys. Rev. B* **81**, 224433 (2010).
- 28) M. Tsukano and M. Takahashi, *J. Phys. Soc. Jpn.* **66**, 1153 (1997).
- 29) T. Tonegawa, K. Okamoto, T. Hikihara, and T. Sakai, *J. Phys.: Conf. Ser.* **828**, 012003 (2017).
- 30) K. Sekiguchi and K. Hida, *J. Phys. Soc. Jpn.* **86**, 084706 (2017).
- 31) T. Hikihara, T. Tonegawa, K. Okamoto, and T. Sakai, *J. Phys. Soc. Jpn.* **86**, 054709 (2017).
- 32) S. R. White, *Phys. Rev. Lett.* **69**, 2863 (1992).
- 33) S. R. White, *Phys. Rev. B* **48**, 10345 (1993).
- 34) Z. L. Berezinskii, *Sov. Phys. JETP* **34**, 610 (1971).
- 35) J. M. Kosterlitz and D. J. Thouless, *J. Phys. C* **6**, 1181 (1973).
- 36) K. Nomura and A. Kitazawa, *J. Phys. A* **31**, 7341 (1998).
- 37) M. P. Nightingale, *Physica A* **83**, 561 (1976).
- 38) The four-rung-period oscillation in $\omega_\ell^{zz,0}(j;96,0)$ found in Fig. 12 can be understood as follows. Let d (d') be the distance between the j_0 th [$(j_0 + j)$ th] rung and the left (right) edge of the open ladder. Then, as j increases, the parity of (d, d') changes as \dots , (even, even), (even, odd), (odd, odd), (odd, even), \dots .
- 39) T. Giamarchi, *Quantum Physics in One Dimension* (Oxford University Press, New York, 2004).
- 40) The reason why we show the results for a rather small system with $L=32$ here is as follows. In the Néel phase, the finite system has a unique ground state, which is represented by a bonding or antibonding state of the two lowest-energy states in the subspace of $M=0$, and the local magnetization is zero, namely, $m_\ell^0(j;L,M)=0$. However, in the DMRG calculation, one of the two lowest-energy states is selected (depending on a randomly prepared initial state) for a finite but large system, resulting in the nonzero local magnetization $m_\ell^0(j;L,M)\neq 0$ even for $M=0$. Indeed, we have obtained such a ground state with nonzero $m_\ell^0(j;L,M)$ for $L\geq 48$. Although this observation of $m_\ell^0(j;L,M)\neq 0$ for large systems can also be regarded as an indication of the Néel phase, we have restricted ourselves to treating the rather small systems with $L\leq 32$, which preserve $m_\ell^0(j;L,M)=0$.
- 41) J. H. Cardy, *J. Phys. A* **17**, L385 (1984).
- 42) J. Des Cloizeaux and M. Gaudin, *J. Math. Phys.* **7**, 1384 (1966).
- 43) J. D. Johnson, S. Krinsky, and B. McCoy, *Phys. Rev. A* **8**, 2526 (1973).